Interface-Dominated Topological Transport in Nanograined Bulk Bi$_2$Te$_3$

Sepideh Izadi, Jeong Woo Han, Sarah Salloum, Ulrike Wolff, Lauritz Schnatmann, Aswin Asaithambi, Sebastian Matschy, Heike Schlörb, Heiko Reith, Nicolas Perez, Kornelius Nielsch, Stephan Schulz, Martin Mittendorff, and Gabi Schierning*

3D topological insulators (TI) host surface carriers with extremely high mobility. However, their transport properties are typically dominated by bulk carriers that outnumber the surface carriers by orders of magnitude. A strategy is herein presented to overcome the problem of bulk carrier domination by using 3D TI nanoparticles, which are compacted by hot pressing to macroscopic nanograined bulk samples. Bi$_2$Te$_3$ nanoparticles well known for their excellent thermoelectric and 3D TI properties serve as the model system. As key enabler for this approach, a specific synthesis is applied that creates nanoparticles with a low level of impurities and surface contamination. The compacted nanograined bulk contains a high number of interfaces and grain boundaries. Here it is shown that these samples exhibit metallic-like electrical transport properties and a distinct weak antilocalization. A downward trend in the electrical resistivity at temperatures below 5 K is attributed to an increase in the coherence length by applying the Hikami–Larkin–Nagaoka model. THz time-domain spectroscopy reveals a dominance of the surface transport at low frequencies with a mobility of above 10^3 cm^2 V^{-1} s^{-1} even at room temperature. These findings clearly demonstrate that nanograined bulk Bi$_2$Te$_3$ features surface carrier properties that are of importance for technical applications.

1. Introduction

TIs are a class of quantum materials characterized by the appearance of Dirac carriers at the surfaces of the material.[1,2]

3D TIs feature a bulk band gap of a conventional semiconductor and topological surface states on all crystal facets.[3] Electrons on these topological surface states are robust with respect to localization.[4] Even with strong disorder on the atomic scale, these electrons do not backscatter between states of opposite momentum and opposite spin.[5] This confers the high mobility of the electrons occupying these surface states. Such electrons also penetrate energetic barriers caused by materials imperfections and atomic steps at the surfaces.[4] These unique electronic properties propel visions of potential applications in quantum computing and spintronics.[6]

Tetradymite-type bismuth telluride, Bi$_2$Te$_3$, is a famous representative of 3D TIs. However, its defect chemistry is rather complex. For instance, slight changes in the material stoichiometry defined by anti-site defects[7] and disorders[8] determine the dominant carrier transport mechanism. The n-type semiconducting behavior can be attributed to naturally occurring Te-vacancies that donate two electrons each. Additionally, anti-site defects of Te-atoms on Bi-lattice sites lead to intrinsic n-type doping of these materials.[9] According to a density functional theory

S. Izadi, L. Schnatmann, G. Schierning
Bielefeld University
Faculty of Physics
Experimental Physics
33615 Bielefeld, Germany
E-mail: gabi.schierning@uni-bielefeld.de
S. Izadi, U. Wolff, L. Schnatmann, H. Schlörb, H. Reith,
N. Perez, K. Nielsch
Leibniz IFW Dresden
Institute for Metallic Materials
01069 Dresden, Germany

J. W. Han, A. Asaithambi, S. Matschy, M. Mittendorff
University of Duisburg-Essen
Faculty of Physics
47057 Duisburg, Germany
S. Salloum, S. Schulz
University of Duisburg-Essen
Faculty of Chemistry
45141 Essen, Germany
L. Schnatmann, K. Nielsch
Institute of Applied Physics
TU Dresden
01062 Dresden, Germany
K. Nielsch
Institute of Materials Science
TU Dresden
01062 Dresden, Germany

calculation of the role of defects in Bi_2Te_3 material,[10] E_F is shifted toward the valence band or conduction band by excess amount of Bi or Te, respectively, resulting in an enhanced density of states near E_F. The bulk carrier density, n_B, in Bi_2Te_3 is approximately 10^{18} to 10^{19} cm^{-3}, Ref. [11]. Since the chemical potential, μ, defines both bulk and surface states, the resulting surface carrier density, n_s, is much smaller, typically in the order of 10^{12} cm^{-2}, Refs. [12,13]. As in bulk crystals, the surface to volume ratio is typically small; electrons that contribute to the bulk band transport usually dominate over surface electrons in their quantity by orders of magnitude.[1]

It is technologically challenging to reduce μ by fabricating Bi_2Te_3 bulk close to a theoretically predicted intrinsic carrier density of 10^{16} cm^{-3} Ref. [14]. In a material with a sufficiently decreased bulk carrier density by compensational doping, the contribution of surface states to the DC conductivity, σ, was increased[12,15] but only to 6% at 1.6 K.[12] The transition to single isolated nanoobjects[16,17] increased the surface to volume ratio, therewith maximizing the contribution of surface states. Nanowires[18] and thin films[19] revealed evidence of surface states with high charge carrier mobility and small Seebeck coefficients. These surface states lead to the counterintuitive behavior that a reduced grain size results in an increase in charge carrier mobility, also in nanograined bulk.[20] The accompanying reduction of the Seebeck coefficient, in a similar fashion as in nanowires or thin films, further indicates the contribution of surface states in those bulk samples.[16]

In addition, recent theoretical studies predict the feasibility of topologically protected transport channels in bulk TIs, mediated by defects like stacking faults, dislocations, and even point defects.[21–23] These defect-mediated topological transport channels can easily be envisioned to create a percolating 3D network within a bulk material given favorable number and conditions of geometrical arrangement. Based on these considerations, we here present the well-known approach of nanograined bulk material,[24–26] but utilized it for 3D TI transport, conceptually sketched in **Figure 1**. Such nanograined bulk materials contain a high number of thermodynamically-stable interfaces and grain boundaries introducing considerable barriers toward charge carrier transport.[27] Within this work, we investigate these kinds of interfaces for their effectivity in promoting surface transport. Nanoparticles were synthesized using tailored precursors in ionic liquids to ensure high stoichiometry and low level of contamination. They were compacted to a macroscopic bulk pellet producing a percolating network of Dirac carriers on interfaces and grain boundaries. Clear experimental evidence of the dominance of Dirac carriers over bulk carriers was found at temperatures up to 150 K, and still remaining significant at room temperature, measured by time-domain THz spectroscopy.

2. Results and Discussion

Topological transport in 3D TIs is governed by surface charge carriers that are characterized by a linear dispersion relation of Dirac cones, i.e., the charge carrier velocity is independent of the energy. To expand this 2D effect to a 3D bulk, a high number of well-defined surfaces in a 3D arrangement is required. Hereby, it is not important which crystallographic facets are available, but their structural quality and chemical cleanliness need to be excellent. We achieved high purity Bi_2Te_3 nanoparticles by a specific chemical synthesis method using tailor-made precursors that were decomposed in ionic liquids, in the absence of organic surfactants and coordinating solvents.[28]

The chemical composition, phase purity, morphology, and particle surface of the obtained nanomaterials were examined by energy-dispersive X-ray spectroscopy (EDX), powder X-ray diffraction (PXRD), transmission electron microscopy (TEM), and X-ray photoelectron spectroscopy (XPS), as shown in **Figure 2**. According to X-ray diffraction, the Bi_2Te_3 nanoparticles were identified as phase-pure tetradymite-type materials. All observed Bragg reflections can be indexed to the rhombohedral Bi_2Te_3 (PDF 15–863). No additional impurity phases such metal oxides, elemental tellurium, and other Bi_xTe_y phases were observed. Element mapping of the respective TEM image revealed a stoichiometric and homogeneous distribution of tellurium and bismuth within Bi_2Te_3 nanoparticles. The binding energies of the Bi 4f (157.9 eV) and Te 3d (572.5 eV) signals detected in the XPS measurements are in close agreement with those reported for Bi_2Te_3 surfaces.[29] Both XPS and electron-energy-loss spectroscopy (EELS) did not detect the presence of metal-bound oxygen on the material surface, whereas the
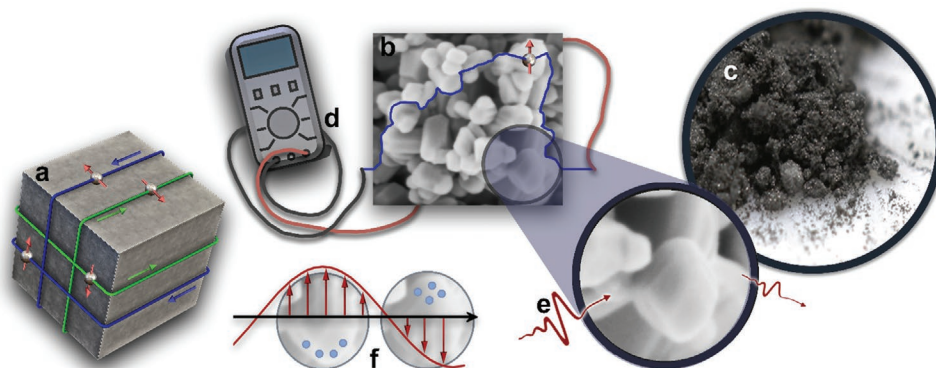

Figure 1. Often, 3D TI properties are experimentally studied using model systems like single crystals or epitaxial thin films (a). Our approach is that of nanograined bulk material (b) from a scalable wet-chemical synthesis (c). Compacted nanoparticles exhibit a percolating network of Dirac carriers on interfaces and grain boundaries, as seen in the DC transport (d). Time-domain THz spectroscopy (e) evidences the dominance of Dirac carriers over bulk carriers by a plasmon resonance (f).
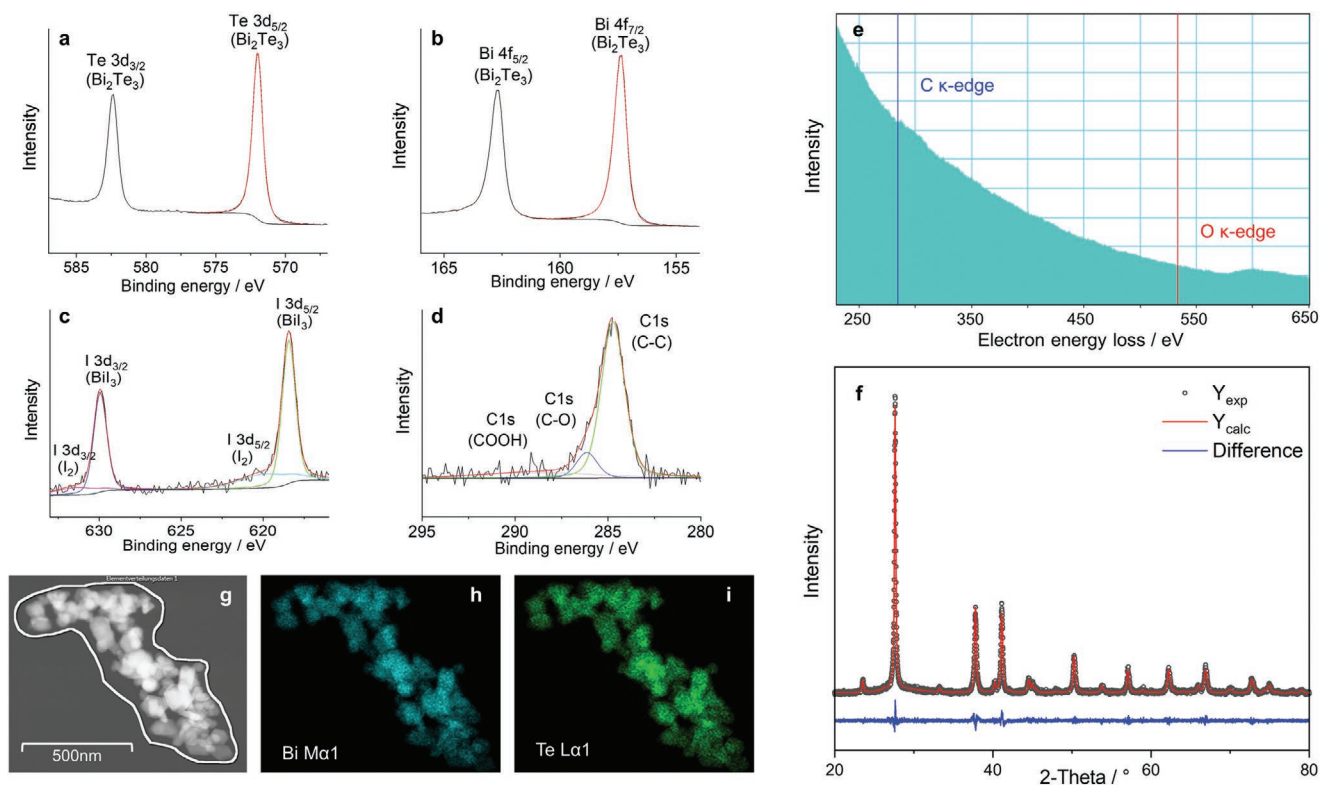
Figure 2. XPS a) Te $3d_{5/2}$ b) Bi $4f_{7/2}$ c) C 1s and d) I 3d signals of Bi_2Te_3 nanoparticles synthesized by reaction of $[C_4C_1Pyr][TeSiEt_3]$ with $[C_4C_1Im][Bi_3I_{12}]$ in $[C_4C_1Im]I$ at 150°C under inert gas. e) EEL spectrum of Bi_2Te_3 nanoparticles under inert gas. Regions in which signals due to carbon and oxygen are expected are indicated. g) TEM image of Bi_2Te_3 nanoparticles with EDX element mapping showing homogenously distributed h) Bi (teal) and i) Te (green). f) PXRD including Rietveld refinement of Bi_2Te_3 powders synthesized by reaction of $[C_4C_1Pyr][TeSiEt_3]$ with $[C_4C_1Im][Bi_3I_{12}]$ in $[C_4C_1Im]I$ at 150°C.

amount of surface-bound organic impurities is significantly reduced in comparison to Bi_2Te_3 nanoparticles synthesized in the presence of organic capping agents.

Figure 3a,b represent TEM and SEM overview images of the initial powder that shows a high degree of agglomeration of the nanoparticles. A high resolution of the initial powder emphasizing their crystallographic integrity is represented in Figure 3c. The average size of the nanoparticles before compaction was around 40 to 50 nm (Figure 3d). The nanoparticles were compacted at mild conditions of around 580 K in a hot press to pellets of diameter 5 mm and thickness 0.5 mm with a mass density of 7.6 gcm^{-3} corresponding to 99% dense Bi_2Te_3 bulk sample (Figure 3e,f). Both the nanoparticle synthesis and all subsequent processing steps were carried out under strict inert gas conditions to produce oxygen-free surfaces. The macroscopic pellets feature an anisotropic lattice thermal conductivity that was close to the theoretical value,[30] proving the high crystalline quality of these pellets despite of their nanograined structure. Details of the synthesis procedures and nanoparticle characterization are given in the supporting online materials (Experimental Section S-I and S-II).

The specific surface area of the nanoparticles and the compacted nanoparticle bulk were determined by gas adsorption experiments with Brunauer-Emmett-Teller method (BET, see Figure S9), yielding a free surface area of 1.8×10^5 cm^2 g^{-1} of the nanoparticles and 2.6×10^4 cm^2 g^{-1} of the compacted pellets. Based on the density of Bi_2Te_3 of 7.7 g cm^{-3} Ref. [31], these pellets

have a surface to volume ratio of approximately 2×10^5 cm^{-2} cm^{-3}. The BET characterization shows that approximately one tenth of the initially available free surfaces are preserved within the compacted bulk.

Figure 3f depicts the compacted Bi_2Te_3 nanoparticles scanned by atomic force microscope (AFM) at room temperature on a cross section of the pellet. The topographic AFM image shows a multi-grained nanoparticle material, evidencing that the initial characteristics of the agglomerated powder are preserved within the compacted pellet. Conductive AFM on the same cross section indicates an enhanced conductivity along the edges and interfaces between the nanoparticles (Figure 3g,h). Note that only percolating conductive channels contribute to the conductive AFM image.

Temperature and magnetic field, B, dependent resistivity, ρ, as well as Hall resistivity were measured in van der Pauw geometry. The temperature dependent ρ (**Figure 4a**) shows a metallic conductivity trend down to a temperature of 5 K. Below 5 K, ρ shows a clear drop (Figure 4a), qualitatively comparable to the behavior of a superconductor. Heat capacity measurements (see supporting online material Figure S10) show no indication of a phase transition in this temperature regime. Therefore, we interpret this drop as an evidence of spin-orbit coupled transport, associated with the phenomenon of weak antilocalization, WAL (Figure 4b).[32] As the magnitude of B increases (Figure 4a,b), the signature of the spin-orbit coupled transport disappears. Such downward trend in ρ was previously reported only for a high
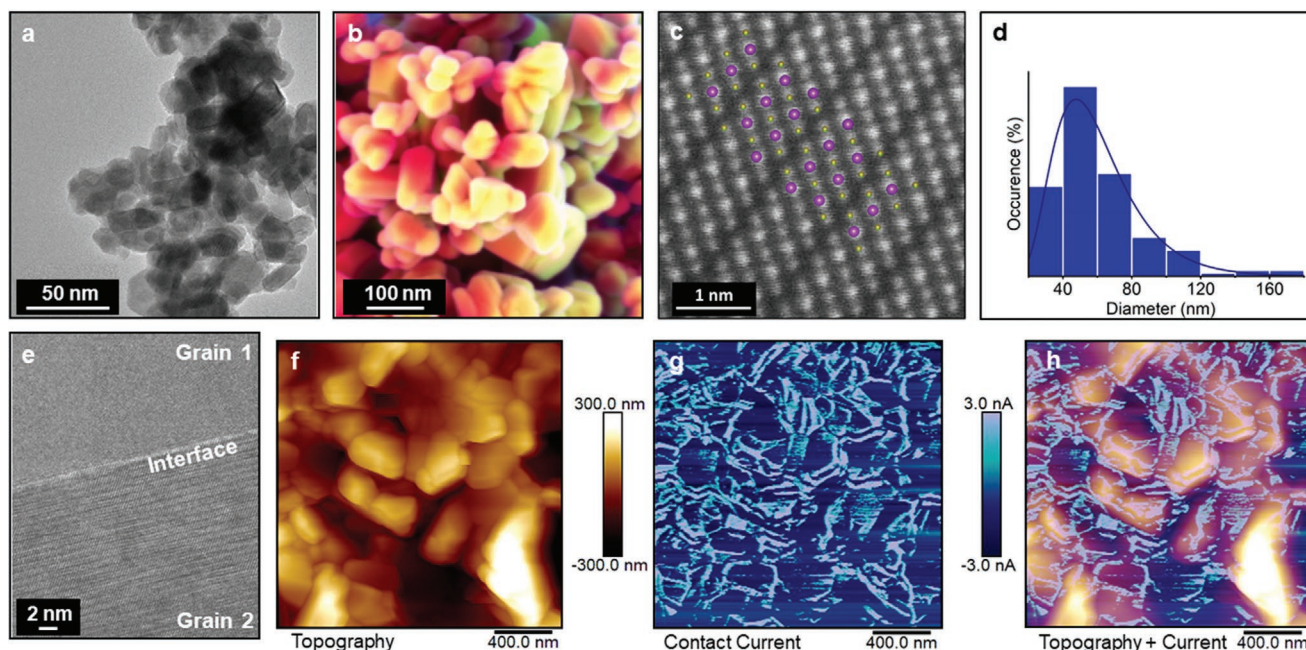
Figure 3. a) TEM image of Bi₂Te₃ nanoparticles, synthesized by reaction of [C1C1Pyr][TeSiEt₃] with [C4mim]₃[Bi₃I₁₂] in [C4C1Im]I at 150°C. b) SEM image of Bi₂Te₃ nanoparticles. c) High-angle annular dark field (HAADF) STEM image of Bi₂Te₃ nanoparticles, and overlay of the model crystal structure of Bi₂Te₃ (purple: Bi, yellow: Te). d) Particle size distribution of Bi₂Te₃ initial nanoparticles. e) High resolution TEM image showing the interface between two grains of a Bi₂Te₃ pellet. f) AFM topography image of the cross section of a Bi₂Te₃ pellet. g) Corresponding contact current image. h) Superposition of the topography and the contact current images.
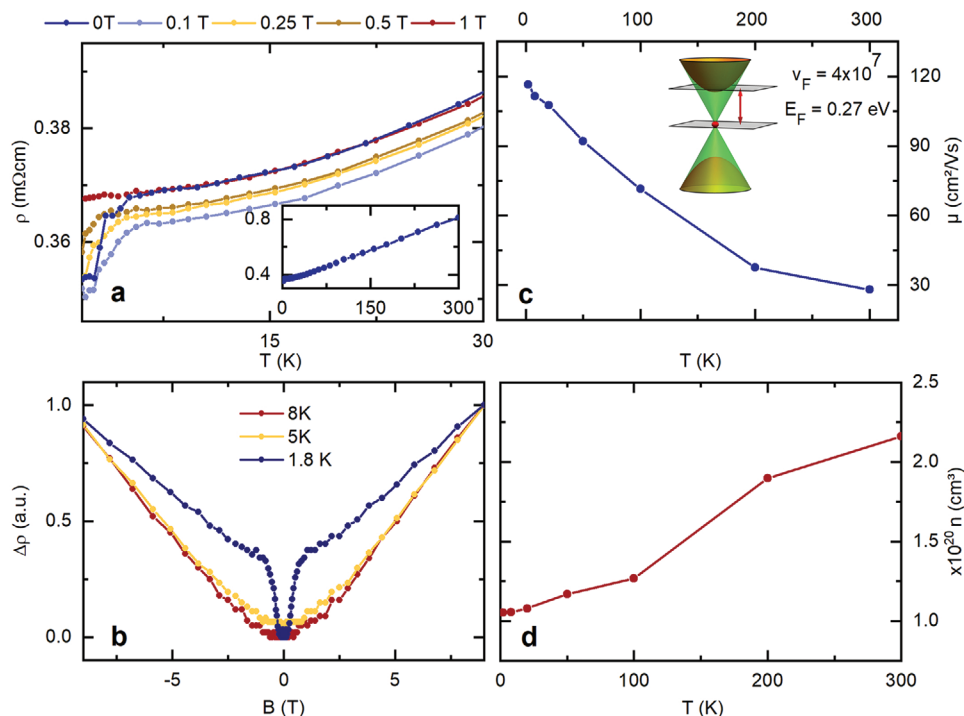

Figure 4. Electrical transport measurement of Bi₂Te₃. a) Resistivity versus temperature in the low temperature regime up to 30 K with applied magnetic field up to 1 T (inset: resistivity versus temperature for 99% dense Bi₂Te₃ bulk sample in the temperature range of 300–1.8 K). b) Comparison of relative resistivity-change versus magnetic field at three different temperatures. c) Bulk carrier mobility in the temperature range 300–1.8 K (inset: Schematic illustration of Bi₂Te₃ band structure). d) Bulk carrier concentration in the temperature range 300–1.8 K.

ADVANCED
SCIENCE NEWS
www.advancedsciencenews.com

NANO · MICRO
small
www.small-journal.com

purity epitaxial Bi_2Te_3 film with a reduced bulk carrier density,[33] and was attributed to the predominant conductivity channel of the Dirac carriers arising at the surfaces of the TI.

Hall measurements revealed a charge carrier density of 2.2×10^{20} cm^{-3}, as well as a charge carrier mobility of 28 cm^2 V^{-1} s^{-1} (Figure 4c, (d)) at room temperature, that are predominately related to the bulk carriers. Based on the Hall measurements, we calculated the values of the mean free path of the electrons, l_e, at 300 K and 10 K, respectively. Assuming only bulk carrier transport, the calculated l_e values were 0.7 nm and 2 nm. The average particle size distribution of ~ 40 nm (Figure 3d) suggests that the main scattering mechanism is most likely not dominated by grain boundary scattering, even though a nanograined material was chosen (Figure 3f). Detailed analysis of l_e calculation is provided in supporting online material.

A reproduction sample provided the same characteristic ρ drop along with indication of spin-orbit coupled transport, represented in Figure S12 of supporting online material.

In order to understand the spin-orbit coupled transport causing the downward trend in ρ, we applied a modified 2D Hikami–Larkin–Nagaoka (HLN) quantum interference formula. 2D quantum interference transport was first calculated in the pioneering work of Hikami, Larkin, and Nagaoka,[34] followed by modifications in which a complicated mathematical description of multiple scattering channels was replaced by a simple B^2 term.[35] With these modifications, Equation 1 can be derived. Hereby, the sharp dip of spin-orbit coupled transport in Figure 4b can be interpreted as a positive quantum correction known as WAL effect. Based on this HLN model, magnetoconductance of our nanograined bulk material can be quantified using the following equation:[35]

$$\Delta G_{2D} = \frac{\alpha e^2}{2\pi h}\left[\psi\left(\frac{1}{2} + \frac{B_\phi}{B}\right) - \ln\left(\frac{B_\phi}{B}\right)\right] - cB^2 \qquad (1)$$

B_ϕ and ψ represent characteristic field and digamma function, respectively, while α is a prefactor. Due to dominance of phase coherence length (l_φ) at low temperatures and small magnetic fields, B_ϕ is considered as characteristic field in quantum diffusion transport regime $\left(B_\phi = \frac{\hbar}{4el_\phi^2}\right)$. Subsequently, elastic scattering of mean free path (l_e)—compare discussion

based on the Hall data—and spin-orbit scattering contribution of the bulk carriers are well approximated by the B^2 term.[35,36]

Based on this approximation magnetoconductance (ΔG) of the nanograined Bi_2Te_3 bulk at $T = 1.8$ K (**Figure 5a**) can be well fitted using the 2D HLN model, therewith, l_φ of 107 nm was calculated at $T = 1.8$ K. Considering the high number of scattering barriers of elastic l_e, spin-orbit coupled scattering channel and electron-impurity interactions, l_φ at $T = 1.8$ K is approximately half of the calculated value for epitaxial thin film samples.[37] The corresponding analysis at $T = 5$ K and $T = 50$ K are provided in supporting online material. The sharp dip of the WAL is clearly seen in the 1.8 K magnetoconductance. At 5 K and 50 K, the magneto-conductance is dominated by the quadratic part of Equation 1. The temperature dependence of l_φ at the different temperatures is provided in Figure 5b. l_φ hereby changes clearly from ~24 nm to ~107 nm. This trend, which is consistent with previous reports,[35,38] could provide an explanation for the observed downward trend below 5 K in ρ (Figure 4a).

The prefactor α in the HLN formula defined as WAL coefficient signifies the number of topologically independent conducting channels. Theoretically, $\alpha = -0.5$ is reported for one single topological surface.[34] Considering multiple conducting channels as well as a significant bulk carrier contribution, α can be assumed much higher. We calculated α of 10^5 which is in the same order of magnitude for a Bi_2Te_3 single crystal.[39]

The findings presented so far give clear evidence that bulk band and surface topological transport mechanisms are present within this nanograined material. Their individual contributions were elucidated in more detail by THz time-domain spectroscopy.[40–45] A short THz pulse that is generated by a photoconductive antenna is guided to the sample with two parabolic mirrors, the reflected THz radiation is then collected by another set of two parabolic mirrors and focused to the detector. Like the emitter, the detector is gated by an ultrashort near-infrared pulse, which allows sampling of the electric field evolution of the THz pulse. By calculating the Fourier transform of the measured THz pulse shape, the reflectivity of the sample in a broad spectral range is obtained. In contrast to DC measurements, THz reflectivity gives insights into the carrier density and mobility without the need for additional parameters like the magnetic field for Hall
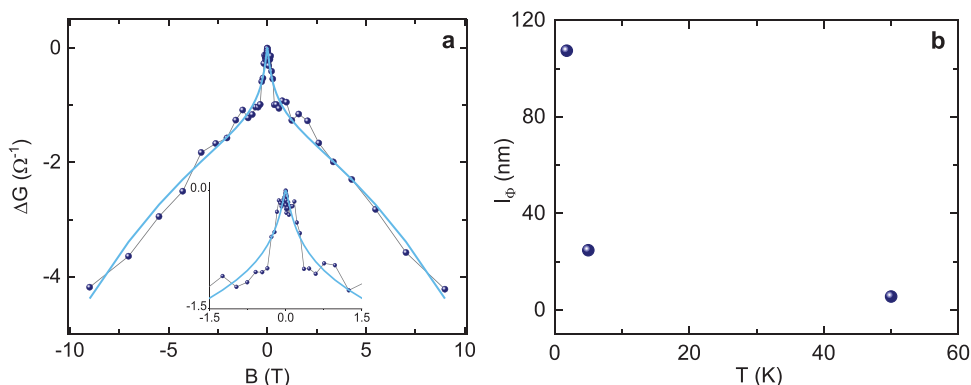

Figure 5. Magnetoconductance fitting based on HLN approach. a) Magnetoconductance versus magnetic field at T = 1.8 K of 97% dense Bi_2Te_3 bulk; Magnified image of magnetoconductance cusp around zero magnetic field is represented in the inset. b) Phase coherence length at three different temperatures.

measurements. Furthermore, different conduction channels can potentially be distinguished spectrally, e.g. if carriers with very different mobility contribute to the net conductivity.

The reflection as a function of the wavenumber and the temperature is shown in the color-coded plot in **Figure 6a**. While the reflection at room temperature is rather flat, a clear dip at around 35 cm⁻¹ can be observed at 4 K.

To further analyze the obtained spectra, we employed a model based on three contributions: free carrier absorption by the bulk and surface carriers, as well as a plasmonic contribution of the surface carriers. The latter is attributed to collective charge carrier oscillations due to the microscopic structure of

the Bi_2Te_3 nanoparticles. Therewith, when the frequency of the electric field is resonant to the plasmon, a strong increase in light–matter interaction occurs. The plasmon frequency depends on the lateral dimensions of the microscopic structure as well as the carrier density.[46] Similar intrinsic THz plasmons occur in graphene layers with natural nanoscale inhomogeneities.[47]

The THz conductivity σ_f^B of the bulk carriers is calculated via the Drude model:

$$\sigma_f^B(\omega) = \frac{n_B p' e^2 \tau_B}{m^*} \left(\frac{1}{1 - i\omega\tau_B} \right) \quad (2)$$
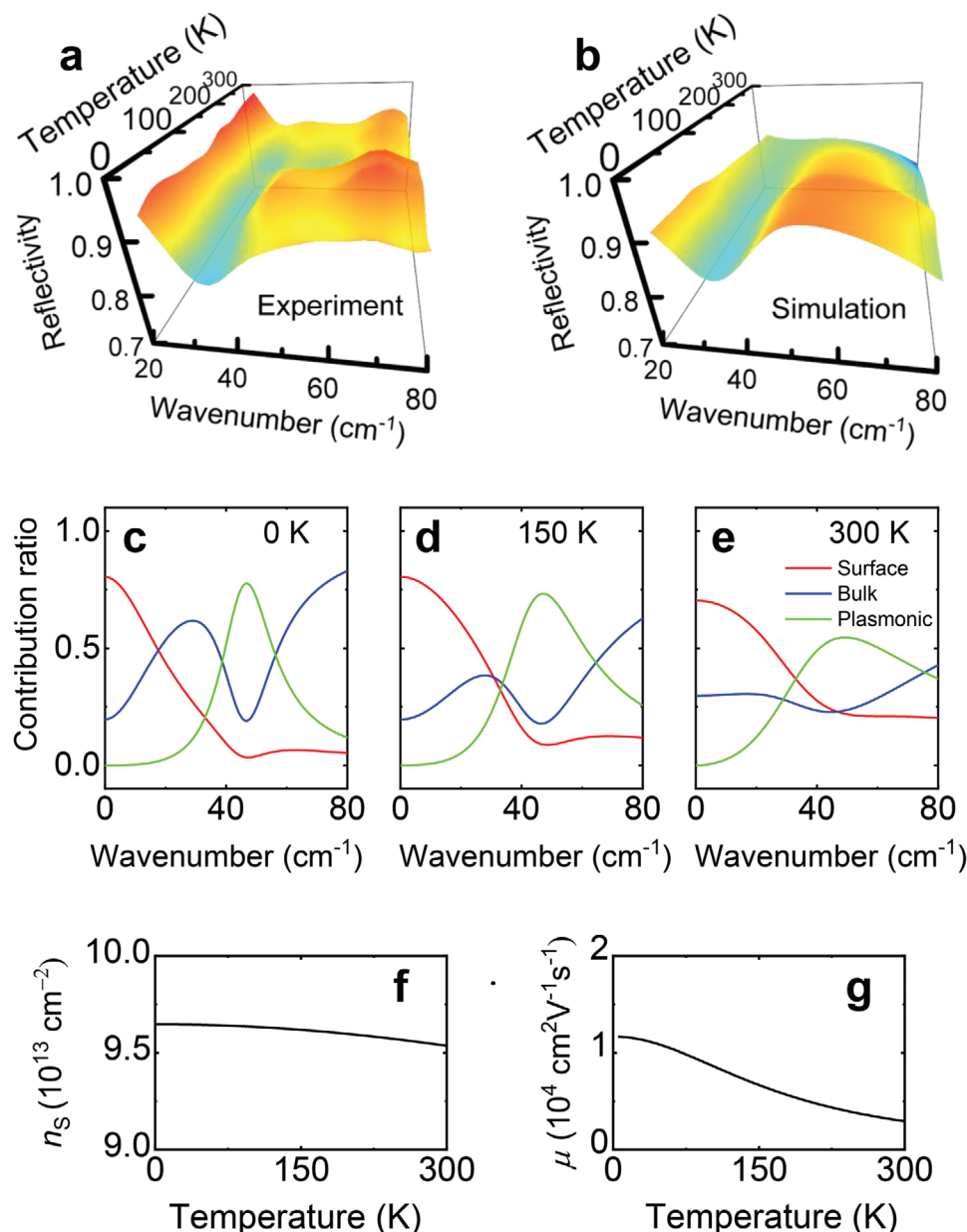

Figure 6. a) Experimentally obtained reflectivity as a function of the wavenumber and temperature in the range of 4 K to 300 K. b) Calculated reflectivity, taking into account bulk and surface Drude conductivity as well as the surface plasmonic contribution. c–e) Ratio of the three different conductivity contribution, namely surface and bulk Drude conductivity as well as plasmonic surface carriers, as a function of the wave number at 0 K, 150 K and 300 K, respectively. f) Surface carrier concentration and g) mobility extracted from the model as a function of temperature.

where n_B represents the bulk carrier density taken from the Hall measurements, e the elementary charge, and τ_B the momentum scattering time of the bulk carriers. The effective mass m^* is the mean value for conduction bands of 0.07 times the electron mass.[48,49] A scaling parameter p' was included taking into account that the sample is not a bulk crystal. The best match between model and measurement was found at $p' = 0.3$. As the surface carriers behave like Dirac carriers, the Drude formula slightly differs from the one for bulk carriers:[43]

$$\sigma_f^S(\omega) = \frac{iq'e^2\sqrt{\pi n_S}v_F}{\pi\hbar(i\gamma_S + \omega)} \tag{3}$$

The surface carrier density n_S was derived from the n_B and the band structure of bulk Bi_2Te_3,[50] leading to a Fermi energy, E_F, that is 0.27 eV above the Dirac point, which is in good agreement with literature.[3] Assuming a Fermi velocity, v_f, of 4×10^7 cm s^{-1} the surface carrier density is calculated[51] to be about 9.6×10^{13} cm^{-2} and only slightly depends on the temperature, which is consistent with earlier reports.[52–54] The scattering rate served as fitting parameter and was set to $\gamma_S = 3 \times 10^{11}$ s^{-1} at 0 K, which corresponds to a mobility of 10^4 cm Vs^{-1}. For elevated temperatures, we assume that the scattering rate increases with the square of the temperature (see supporting online material). This scattering rate is consistent with earlier studies on relativistic quasi particles[52,53,55] and implies a long mean-free path of about 1.3 µm. Note that the surface carriers are topologically protected, which suppresses back scattering at grain boundaries and defects.[53]

From the surface carrier density, we calculate a volumetric carrier density via a surface to volume ratio q' of 2×10^2 cm^{-2} cm^{-3}, which serves as a fitting parameter. This fitted surface to volume ratio is one per mill of the value obtained by BET measurements. It accounts for the fact that most surfaces and interfaces will not be part of a percolating 3D network, which is in qualitative agreement with the conductive AFM measurements (Figure 3g). The plasmonic response caused by the microscopic structure of the nanoparticles was calculated via a modified Drude model:[56]

$$\sigma_P^S(\omega) = \frac{iq'e^2\sqrt{\pi n_S}v_F}{\pi\hbar\left(i\gamma_S + \dfrac{\omega^2 - \omega_P^2}{\omega}\right)} \tag{4}$$

where ω_P represents the plasmon frequency of 1.35 THz, which served as a free parameter to fit the calculated results to the experimentally obtained data. To calculate the reflection spectrum from the three conductivity channels, the frequency dependent permittivity ε is calculated via[50]

$$\varepsilon(\omega) = \varepsilon_\infty + \frac{i(\sigma_f^S + \sigma_f^B + \sigma_P^S)}{\omega\varepsilon_0} \tag{5}$$

with the vacuum permittivity ε_0 and the background permittivity[57] without electron contribution $\varepsilon_\infty = 64$. The charge carrier density and mobility were assumed to be temperature dependent. Details on the calculations of reflectivity spectra as a function of the temperature are provided in the Supporting online material. The temperature and wavenumber dependent

reflectivity calculated with this simple model is shown in Figure 6b. To provide a better insight of the roles of each of the conduction channels, we plotted the ratio of the contributions in Figure 6c–e. The plasmonic contribution is zero for DC measurements and peaks at the resonance frequency (Supporting online material Figure S15 (a)). With increasing temperature, the plasmonic contribution decreases and widens, which is caused by the increase in scattering at elevated temperature. While the bulk carriers dominate the reflection above the plasmon frequency, the surface Drude conductivity dominates below the plasmon frequency, even though the carrier density of the surface carriers is far below the one of the bulk carriers; this holds even true at room temperature as they account for roughly 60% of the conductivity. A more detailed view on the different contributions can be found in the online supplement.

Note that the characteristic dip at 35 cm^{-1} cannot be reproduced by only assuming surface and bulk Drude contributions, but instead requires a resonant behavior connected to a high mobility. Such high mobility can be excluded for the bulk carriers but is offered in the sub-system of surface carriers. The calculated surface carrier density as well as the mobility as a function of the temperature are shown in Figure 6f,g, respectively. As the temperature decreases, the mobility of the surface carriers reaches $\sim 1.2 \times 10^4$ cm^2 V^{-1} s^{-1}. This mobility is in the range of previous reports for the mobility of surface carriers, emphasizing the high quality of the nanoparticles.[52,53,55]

3. Conclusion

Topologically protected surface states offer a variety of outstanding properties that are promising for many technological applications, e.g. spintronics or thermoelectricity. With increasing size, it gets more and more difficult to observe surface states as it is challenging to distinguish between surface and bulk carriers, which tend to dominate the electronic properties of large-scale samples. Our work shows an accessible and pragmatic way of producing macroscopic TI materials that have a clear signature of the surface states and may pave the path toward the fabrication of TI materials, even on an industrial scale. The key to obtaining the samples is to synthesize nanoparticles with clean surfaces and to preserve the nanoparticle character in the bulk. While often the investigation of surface states requires atomically clean surfaces of experimental model systems, we showed that a "real-world" sample actually exhibits the desired properties.

4. Experimental Section

Synthesis: Bi_2Te_3 nanoparticles were synthesized in an ionic-liquid based procedure under strict inert gas conditions using a modified synthetic route from a previously described method (see electronic supplement). In this work, an ethyl variant [C_1C_1Pyr][$TeSiEt_3$] of the previously used reactive telluride precursor was applied instead due to its higher chemical stability, which further ensures the formation of highly stoichiometric materials free of Te-rich phases. To further remove any organic surface impurities, the nanoparticles were repeatedly washed (10x) with acetonitrile and chloroform, and then thermally treated at 300 °C for 12 h under dynamic vacuum at 10^{-6} mbar.

**ADVANCED
SCIENCE NEWS**

www.advancedsciencenews.com

**NANO · MICRO
small**

www.small-journal.com

Nanoparticle Processing: To fabricate macroscopic nanoparticle based Bi_2Te_3, 0.07 g Bi_2Te_3 nanoparticles were compacted for 90 minutes at a temperature of 580 K with a pressure of 2 kN in an inert atmosphere using a mild hot-pressing approach. The hot-pressing tool was incorporated into a glove box system to avoid surface oxidation. To avoid contamination during the compaction procedure, nanoparticles were covered from both sides with tungsten foils. After 2 h of cooling time, the resulting bulk pellet has a thickness of 0.5 mm with diameter of 5 mm.

Transport Characterization: For electrical DC measurements, the pellet shown in Figure 4 was contacted by soldering with a low melting point indium-tin eutectic alloy. Indium-tin was mechanically soldered on gold contact pads of a glass substrate prepared by photolithography. Due to the van der Pauw geometry of the measurement and the macroscopic size of the sample, we assumed that proximity effects as were discussed for isolated Bi_2Te_3 flakes contacted with superconducting indium[58] were negligible. To avoid spurious effects by the contact material, the sample shown in Figure 5 was directly contacted to a puck via four metallic contact probes made of a gold-coated copper beryllium alloy (photograph see supporting online material Figure S14). Electrical properties of the Bi_2Te_3 pellet were characterized in a Physical Property Measurement System (PPMS) of the DynaCool series from Quantum Design between a temperature of 1.8 K and 300 K and a magnetic field B of up to ±9 T.

THz Spectroscopy: THz spectroscopy was performed with a commercial THz time-domain system in reflection geometry. At the sample position, the THz spot size is about 1 mm for frequencies of 1 THz and above, for lower frequencies the spot size was increased according to the wavelength. The sample was mounted next to a gold mirror that served as reference in a closed cycle cryostat to vary the temperature in the range of 4 K to 300 K. Z-cut quartz windows were in place, limiting the upper frequency of the measurement to about 3 THz. Sample and reference mirror were mounted behind apertures with a diameter of 3 mm, limiting the lower threshold for reliable measurements to about 0.7 THz. Multiple measurements taken on different days were averaged to minimize the noise in the data, the observed features were well reproducible.

Derivation of Surface Carrier Density: To extract the surface carrier concentration theoretically from the Hall measurement, we first obtained the Fermi-energy by considering the carrier density extracted from the Hall measurement at the lowest temperature of $\sim 2\,K$, $n_H(2\ K)$, using $\int_{E_c}^{\infty} D(E) \times f(E,E_F)dE + \int_{-\infty}^{E_c} D(E) \times (1 - f(E,E_F))dE = n_H(2\,K)$, where, E_c, $D(E)$, $f(E, E_F)$, and E are the energy of the conduction band minimum, density of states, Fermi-Dirac distribution function, and energy, respectively. E_F turns out to be 0.27 eV above the Dirac point and 0.05 eV above the conduction band minimum. To estimate the temperature-dependent chemical potential of $\mu(T)$, we utilized conservation law for the fixed number of particles, i.e., $\int_{-\infty}^{\infty} D(E) \times f(E,\mu(T))dE = $ constant.

For the bulk carriers, the temperature-dependent carrier density was calculated via $\int_{E_c}^{\infty} D(E) \times f(E,\mu(T))dE + \int_{-\infty}^{E_c} D(E) \times (1 - f(E,\mu(T)))dE = n_B$. The calculated results closely match with the Hall measurements (Figure S14(c)). Finally, we derived surface carrier density from the calculated chemical potential and linear density of states of $D_{2D}(E) = \dfrac{2|E|}{\pi \hbar^2 v_F^2}$, where we assumed that the surface electronic band is linear with v_F being 4×10^7 cm s^{-1}.

Supporting Information

Supporting Information is available from the Wiley Online Library or from the author.

Acknowledgements

Conflict of Interest

The authors declare no conflict of interest.

Author Contributions

S.I., J.W.H., S.S. contributed equally to this work. G.S. conceived the concept. Sa.S. synthesized the nanoparticles, St.S. conceived the synthetic strategy. S.I. together with H.S. fabricated the pellets from the nanoparticles; S.I. performed the DC transport characterization and analyzed the data, supported by L.S., H.R., N.P., and K.N.; U.W. performed the TEM and AFM characterization. J.W.H., A.A., and S.M. performed the THz experiments, J.W.H. and M.M. analyzed the data. G.S. and M.M. wrote the manuscript with contributions from all authors. All authors discussed the results and commented on the manuscript.

Data Availability Statement

Research data are not shared.

Keywords

[1] Y. Ando, *J. Phys. Soc. Jpn.* **2013**, *82*, 102001.
[2] M. Z. Hasan, C. L. Kane, *Rev. Mod. Phys.* **2010**, *82*, 3045.
[3] H. Zhang, C.-X. Liu, X.-L. Qi, X. Dai, Z. Fang, S.-C. Zhang, *Nat. Phys.* **2009**, *5*, 438.
[4] J. Seo, P. Roushan, H. Beidenkopf, Y. S. Hor, R. J. Cava, A. Yazdani, *Nature* **2010**, *466*, 343.
[5] P. Roushan, J. Seo, C. V. Parker, Y. S. Hor, D. Hsieh, D. Qian, A. Richardella, M. Z. Hasan, R. J. Cava, A. Yazdani, *Nature* **2009**, *460*, 1106.
[6] S. Bhatti, R. Sbiaa, A. Hirohata, H. Ohno, S. Fukami, S. N. Piramanayagam, *Mater. Today* **2017**, *20*, 530.
[7] N. K. Singh, J. Pandey, S. Acharya, A. Soni, *J. Alloys Compd.* **2018**, *746*, 350.
[8] A. Soni, Y. Shen, M. Yin, Y. Zhao, L. Yu, X. Hu, Z. Dong, K. A. Khor, M. S. Dresselhaus, Q. Xiong, *Nano Lett.* **2012**, *12*, 4305.
[9] S. Cho, Y. Kim, A. Divenere, G. K. Wong, J. B. Ketterson, J. R. Meyer, *Appl. Phys. Lett.* **1999**, *75*, 1401.
[10] A. Hashibon, C. Elsässer, *Phys. Rev. B: Condens. Matter Mater. Phys.* **2011**, *84*, 14.

[11] H. Cao, R. Venkatasubramanian, C. Liu, J. Pierce, H. Yang, M. Z. Hasan, Y. Wu, Y. P. Chen, *Appl. Phys. Lett.* **2012**, *101*, 162104.

[12] P. Ngabonziza, M. P. Stehno, H. Myoren, V. A. Neumann, G. Koster, A. Brinkman, *Adv. Electron. Mater.* **2016**, *2*, 1600157.

[13] X. Yu, L. He, M. Lang, W. Jiang, F. Xiu, Z. Liao, Y. Wang, X. Kou, P. Zhang, J. Tang, *Nanotechnology* **2013**, *24*, 015705.

[14] N. Bansal, M. R. Cho, M. Brahlek, N. Koirala, Y. Horibe, J. Chen, W. Wu, Y. D. Park, S. Oh, *Appl. Phys. Lett.* **2014**, *104*, 1343.

[15] S. S. Hong, J. J. Cha, D. Kong, Y. Cui, *Nat. Commun.* **2012**, *3*, 757.

[16] J. Gooth, G. Schierning, C. Felser, K. Nielsch, *MRS Bull.* **2018**, *43*, 187.

[17] H. S. Shin, B. Hamdou, H. Reith, H. Osterhage, J. Gooth, C. Damm, B. Rellinghaus, E. Pippel, K. Nielsch, *Nanoscale* **2016**, *8*, 13552.

[18] B. Hamdou, J. Gooth, A. Dorn, E. Pippel, K. Nielsch, *Appl. Phys. Lett.* **2013**, *103*, 193107.

[19] N. F. Hinsche, S. Zastrow, J. Gooth, L. Pudewill, R. Zierold, F. Rittweger, T. Rauch, J. Henk, K. Nielsch, I. Mertig, *ACS Nano* **2015**, *9*, 4406.

[20] G. L. Sun, L. L. Li, X. Y. Qin, D. Li, T. H. Zou, H. X. Xin, B. J. Ren, J. Zhang, Y. Y. Li, X. J. Li, *Appl. Phys. Lett.* **2015**, *106*, 053102.

[21] R. Queiroz, I. C. Fulga, N. Avraham, H. Beidenkopf, J. Cano, *Phys. Rev. Lett.* **2019**, *123*, 266802.

[22] Y. Ran, Y. Zhang, A. Vishwanath, *Nat. Phys.* **2009**, *5*, 298.

[23] Z. Ringel, Y. E. Kraus, A. Stern, *Phys. Rev. B: Condens. Matter Mater. Phys.* **2012**, *86*, 045102.

[24] K. Ahn, J. K. Won, Y. K. Kang, C. Hwang, I. Chung, M.-G. Kim, *Curr. Appl. Phys.* **2019**, *19*, 97.

[25] R. J. Mehta, Y. Zhang, C. Karthik, B. Singh, R. W. Siegel, T. Borca-Tasciuc, G. Ramanath, *Nat. Mater.* **2012**, *11*, 233.

[26] P. Dwivedi, M. Miyata, K. Higashimine, M. Takahashi, M. Ohta, K. Kubota, H. Takida, T. Akatsuka, S. Maenosono, *ACS Omega* **2019**, *4*, 16402.

[27] A. Soni, Z. Yanyuan, Y. Ligen, M. K. K. Aik, M. S. Dresselhaus, Q. Xiong, *Nano Lett.* **2012**, *12*, 1203.

[28] M. Loor, S. Salloum, P. Kawulok, S. Izadi, G. Bendt, J. Guschlbauer, J. Sundermeyer, N. Perez, K. Nielsch, G. Schierning, S. Schulz, *Inorg. Chem.* **2020**, *59*, 3428.

[29] H. Bando, K. Koizumi, Y. Oikawa, K. Daikohara, V. A. Kulbachinskii, H. Ozaki, *J. Phys.: Condens. Matter* **2000**, *12*, 5607.

[30] C. Chiritescu, C. Mortensen, D. G. Cahill, D. Johnson, P. Zschack, *J. Appl. Phys.* **2009**, *106*, 073503.

[31] M. Saleemi, M. S. Toprak, S. Li, M. Johnsson, M. Muhammed, *J. Mater. Chem.* **2012**, *22*, 725.

[32] H.-Z. Lu, S.-Q. Shen, *Spintron. VII* **2014**, *9167*, 91672E.

[33] S. De Castro, M. L. Peres, V. A. Chitta, X. Gratens, D. A. W. Soares, C. I. Fornari, P. H. O. Rappl, E. Abramof, N. F. Oliveira, *Mater. Res. Express* **2016**, *3*, 075905.

[34] S. Hikami, *Prog. Theor. Phys.* **1980**, *63*, 707.

[35] C. Shekhar, C. E. ViolBarbosa, B. Yan, S. Ouardi, W. Schnelle, G. H. Fecher, C. Felser, *Phys. Rev. B: Condens. Matter Mater. Phys.* **2014**, *90*, 165140.

[36] B. A. Assaf, T. Cardinal, P. Wei, F. Katmis, J. S. Moodera, D. Heiman, *Appl. Phys. Lett.* **2013**, *102*, 012102.

[37] H. T. He, G. Wang, T. Zhang, I.-K. Sou, G. K. L Wong, J.-N. Wang, H.-Z. Lu, S.-Q. Shen, F.-C. Zhang, *Phys. Rev. Lett.* **2011**, *106*, 166805.

[38] O. Chiatti, C. Riha, D. Lawrenz, M. Busch, S. Dusari, J. Sánchez-Barriga, A. Mogilatenko, L. V. Yashina, S. Valencia, A. A. Ünal, O. Rader, S. F. Fischer, *Sci. Rep.* **2016**, *6*, 27483.

[39] A. Lakhani, D. Kumar, *Appl. Phys. Lett.* **2019**, *114*, 182101.

[40] C. S. Tang, et al., *Sci. Rep.* **2013**, *3*, 3.

[41] B. C. Park, T.-H. Kim, K. I. Sim, B. Kang, J. W. Kim, B. Cho, K.-H. Jeong, M.-H. Cho, J. H. Kim, *Nat. Commun.* **2015**, *6*, 6552.

[42] J. Jamnik, J. R. Kalnin, E. A. Kotomin, J. Maier, *Phys. Chem. Chem. Phys.* **2006**, *8*, 1310.

[43] J. Horng, C.-F. Chen, B. Geng, C. Girit, Y. Zhang, Z. Hao, H. A. Bechtel, M. Martin, A. Zettl, M. F. Crommie, Y. R. Shen, F. Wang, *Phys. Rev. B – Condens. Matter Mater. Phys.* **2011**, *83*, 165113.

[44] J. W. Han, et al., *Opt. Lett.* **2014**, *39*, 195531.

[45] K. Shimakawa, T. Itoh, H. Naito, S. O. Kasap, *Appl. Phys. Lett.* **2012**, *100*, 10.

[46] L. Ju, B. Geng, J. Horng, C. Girit, M. Martin, Z. Hao, H. A. Bechtel, X. Liang, A. Zettl, Y. R. Shen, F. Wang, *Nat. Nanotechnol.* **2011**, *6*, 630.

[47] I. Crassee, M. Orlita, M. Potemski, A. L. Walter, M. Ostler, T. Seyller, I. Gaponenko, J. Chen, A. B. Kuzmenko, *Nano Lett.* **2012**, *12*, 2470.

[48] B. L. Huang, M. Kaviany, *Phys. Rev. B – Condens. Matter Mater. Phys.* **2008**, *77*, 1.

[49] A. Wolos, S. Szyszko, A. Drabinska, M. Kaminska, S. G. Strzelecka, A. Hruban, A. Materna, M. Piersa, *Phys. Rev. Lett.* **2012**, *109*, 247604.

[50] K. Carva, J. Kudrnovský, F. Máca, V. Drchal, I. Turek, P. Baláž, V. Tkáč, V. Holý, V. Sechovský, J. Honolka, *Phys. Rev. B* **2016**, *93*, 214409.

[51] J. Gooth, B. Hamdou, A. Dorn, R. Zierold, K. Nielsch, *Appl. Phys. Lett.* **2014**, *104*, 243115.

[52] D.-X. Qu, Y. S. Hor, J. Xiong, R. J. Cava, N. P. Ong, *Science* **2010**, *329*, 821.

[53] K. Shrestha, et al., *Phys. Rev. B* **2017**, *95*, 1.

[54] Z. Liao, M. Brahlek, J. M. Ok, L. Nuckols, Y. Sharma, Q. Lu, Y. Zhang, H. N. Lee, *APL Mater.* **2019**, *7*, 041101.

[55] F. Xiu, L. He, Y. Wang, L. Cheng, L.-T. Chang, M. Lang, G. Huang, X. Kou, Y. Zhou, X. Jiang, Z. Chen, J. Zou, A. Shailos, K. L. Wang, *Nat. Nanotechnol.* **2011**, *6*, 216.

[56] M. M. Jadidi, J. C. König-Otto, S. Winnerl, A. B. Sushkov, H. D. Drew, T. E. Murphy, M. Mittendorff, *Nano Lett.* **2016**, *16*, 2734.

[57] S. V. Dordevic, M. S. Wolf, N. Stojilovic, H. Lei, C. Petrovic, *J. Phys. Condens. Matter* **2013**, *25*, 075501.

[58] Z. Wang, T. Ye, R. G. Mani, *Appl. Phys. Lett.* **2015**, *107*, 172103.